

# Initial performance studies of a general-purpose detector for multi-TeV physics at a 100 TeV $pp$ collider

S.V. Chekanov<sup>a</sup>, M. Beydler<sup>a</sup>, A.V. Kotwal<sup>b,c</sup>, L. Gray<sup>c</sup>, S. Sen<sup>b</sup>, N.V. Tran<sup>c</sup>,  
S.-S. Yu<sup>e</sup>, J. Zuzelski<sup>d</sup>

<sup>a</sup> *HEP Division, Argonne National Laboratory, 9700 S. Cass Avenue, Argonne, IL 60439, USA.*

<sup>b</sup> *Department of Physics, Duke University, USA*

<sup>c</sup> *Fermi National Accelerator Laboratory*

<sup>d</sup> *Department of Physics, Michigan State University, 220 Trowbridge Road, East Lansing, MI 48824*

<sup>e</sup> *Department of Physics, National Central University, Chung-Li, Taoyuan City 32001, Taiwan*

---

## Abstract

This paper describes simulations of detector response to multi-TeV particles and jets at the Future Circular Collider (FCC-hh) or Super proton-proton Collider (SppC) which aim to collide proton beams with a centre-of-mass energy of 100 TeV. The unprecedented energy regime of these future experiments imposes new requirements on detector technologies which can be studied using the detailed GEANT4 simulations presented in this paper. The initial performance of a detector designed for physics studies at the FCC-hh or SppC experiments is described with an emphasis on measurements of single particles up to 33 TeV in transverse momentum. The reconstruction of hadronic jets has also been studied in the transverse momentum range from 50 GeV to 26 TeV. The granularity requirements for calorimetry are investigated using the two-particle spatial resolution achieved for hadron showers.

*Keywords:* multi-TeV physics,  $pp$  collider, future hadron colliders, FCC, SppC

---

## 1. Introduction

A 100 TeV proton-proton collider leads to many challenges for detector design, and requires an optimized detector in order to achieve its physics goals. The capabilities of such a detector should include the ability to measure parameters of particles and jets in the multi-TeV range. Such challenges exist for future circular  $pp$  colliders of the European initiative, FCC-hh [1] and the Chinese initiative, SppC [2].

A promising starting point for this detector is provided by the Silicon Detector (SiD) [3] concept, that was developed for the International Linear Collider (ILC) [4, 5]. The SiD is a compact, general-purpose detector designed for high-precision measurements of  $e^+e^-$  collisions at a centre-of-mass energy of 500 GeV that can be extended to

---

*Email addresses:* chekanov@anl.gov (S.V. Chekanov), mmbeydler@gmail.com (M. Beydler), ashutosh.kotwal@duke.edu (A.V. Kotwal), lagray@fnal.gov (L. Gray), sourav.sen@duke.edu (S. Sen), ntran@fnal.gov (N.V. Tran), syu@cern.ch (S.-S. Yu), jwzuzelski18@gmail.com (J. Zuzelski)

1 TeV. The choice of silicon sensors for the tracking system and for the electromagnetic calorimeter ensures that the detector is resistant to beam backgrounds, while high-granularity calorimeters are well-suited for the reconstruction of individual particles and hadronic jets. Key characteristics of the SiD detector are summarized in [3]. Together with efficient tracking, the fine segmentation of the calorimeter system optimizes the SiD detector for the use of particle-flow algorithms (PFA) which enables identification and reconstruction of individual particles. The PFA objects can be reconstructed using the software algorithms implemented in the PANDORA package [6, 7].

The detector described and studied in this paper is the Silicon Future Circular Collider (SiFCC) detector which shares many design features with the SiD detector. This novel detector concept was studied using detailed GEANT4 simulation [8], and is suitable for measuring particles and jets up to 30 TeV in transverse momentum ( $p_T$ ).

The unprecedented energy of future experiments imposes new requirements on detector design. The goal of software implementation of the SiFCC detector is to provide a versatile environment for simulations of detector performance, testing new technology options, event reconstruction techniques, as well as for assessment of the impact of specific detector designs on physics. Currently, several versions of the SiFCC detector are available for testing calorimeter and tracking technologies, providing an indispensable tool for the design of the final version of the FCC-hh or SppC detectors.

## 2. Software implementation and Monte Carlo simulations

The response of the SiFCC detector to physics processes has been simulated using the Simulator for the Linear Collider (SLIC) software [9], which was developed for the ILC project. The main strength of this software is the easily configurable detector geometry using XML option files.

One approach for understanding detector effects on physics results is to use “fast” simulations of detector response, implemented in programs such as DELPHES [10], where detector resolution functions and efficiencies are parameterized. In this strategy, the impact of detector technology choices on physics is difficult to assess since the required response functions first need to be parameterized using fundamental principles. The approach used in this paper is based on the GEANT4 toolkit with realistic detector description based the Linear Collider Detector Description (LCDD). It also utilizes the SLIC software packages for realistic reconstruction of tracks and calorimeter clusters. These features make these Monte Carlo simulations indispensable for testing different detector designs from first principles.

The truth-level samples used for detector simulation and reconstruction were created using the ProMC package [11]. The GEANT4 simulation and event reconstruction based on SLIC software are described in [12]. The event samples are available from the HepSim database [13]. All calculations, from event generation to simulation and reconstruction, were performed using the Open Science Grid [14] and Argonne’s Laboratory Computing Resource Center. The creation of the event samples presented in this paper required one million CPU hours.

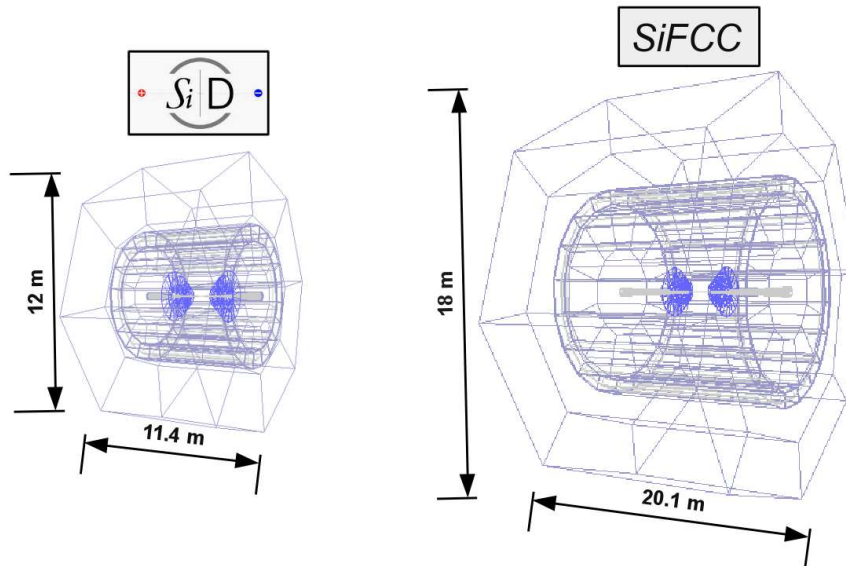


Figure 1: A size comparison of the SiD and SiFCC detectors. See the text for the complete description and other differences.

### 3. Detector description

The software implementation of the SiFCC detector leverages the original SiD detector design. The size of the SiFCC detector has been significantly extended. The total length of the detector has been increased to 20.1 m with an outer radius of 9 m. Figure 1 illustrates the size comparison of the SiFCC detector with the original SiD detector, while Fig. 2 shows the sizes of the SiFCC sub-detectors in the  $x - y$  plane. Figure 3 shows the  $r - z$  view of the detector.

The main characteristics of the SiFCC detector are as follows, including specific differences between the SiFCC and SiD detectors:

- Almost  $4\pi$  solid angle coverage for reconstructed particles.
- A barrel tracker consisting of five layers of silicon sensors with  $50 \mu\text{m}$  pitch. The forward tracker has four disks of silicon sensors.
- Silicon pixel detector with  $20 \mu\text{m}$  pitch, consisting of five layers in the barrel and six disks in the forward region. The pixel detector and the forward tracker are shown in Fig. 4. The tracker was increased in size, and extended in the forward region, compared to the SiD detector in order to provide good measurements of tracks in the  $pp$  collision environment. The tracking coverage up to a pseudorapidity<sup>1</sup> of  $|\eta| = 3.5$  can be achieved.

<sup>1</sup> As for many detectors designed for  $pp$  collisions, the coordinate system of the SiFCC detector is a Cartesian right-handed coordinate system. The nominal beam collision point is at the origin,  $(x, y, z) = (0, 0, 0)$ . The anti-clockwise beam direction around the collider defines the positive  $z$ -axis. The positive  $x$ -axis is defined as pointing radially outwards from the collider ring, and the positive

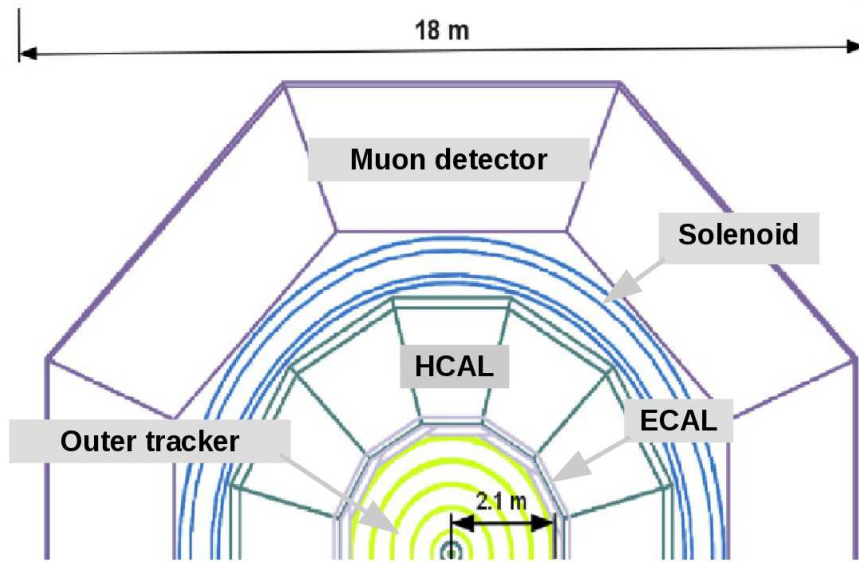


Figure 2: The  $x - y$  view of the SiFCC detector. The inner silicon tracker, with radius of 2.1 m, is surrounded by the electromagnetic and hadronic calorimeters inside the solenoid coil, and the muon detectors on the outside are visible. The abbreviations shown in this figure are explained in Sect. 3.

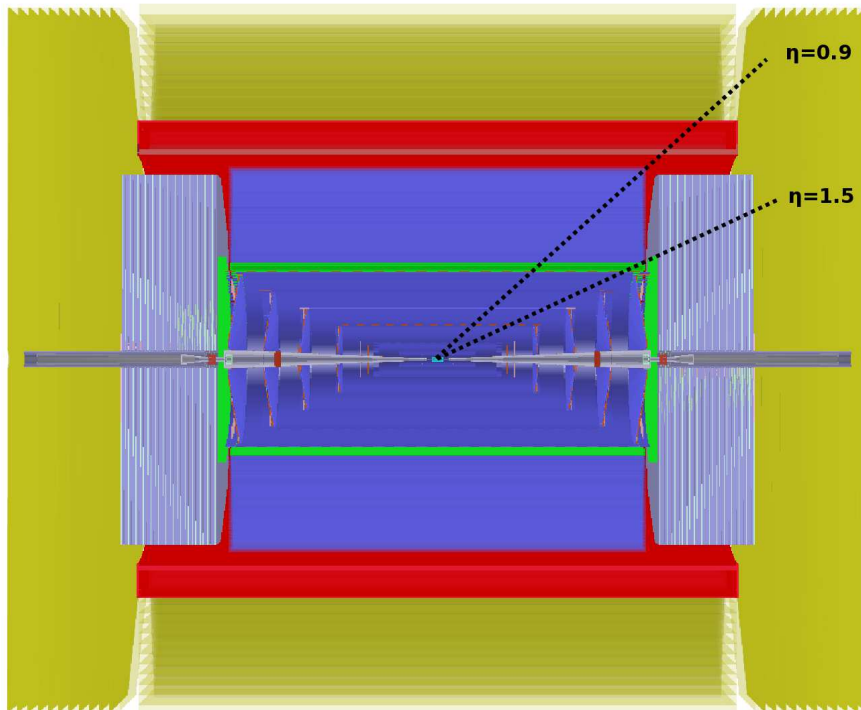


Figure 3: The  $r - z$  view of the SiFCC detector. The solenoid that provides the 5 T magnetic field is shown in red. The electromagnetic calorimeter (ECAL) and the hadronic calorimeter (HCAL) are shown with the green and blue color, respectively. The light blue color from each side of the outer tracker is used to show the HCAL end-cap calorimeter. The inner silicon tracker inside the ECAL is shown in dark blue. The muon spectrometer shown in yellow surrounds the solenoid magnet in the barrel region and the end-cap HCAL.

- Superconducting solenoid with a 5 T field extended in length from the original SiD detector to provide a more uniform magnetic field in the forward region. Note that a 5 T field was also used in the SiD design.
- Highly segmented silicon-tungsten electromagnetic calorimeter (ECAL) with the transverse cell size of  $2 \times 2$  cm. The ECAL has 30 layers built from tungsten pads with silicon readout, corresponding to  $35 X_0$ . The first 20 layers use tungsten of 3 mm thickness. The electromagnetic sampling fraction is 1.47%, as determined from single-photon and single-electron simulation samples by calculating the ECAL energy deposition in the active material. The last ten layers use tungsten layers of twice the thickness, and thus have half the sampling fraction. There are two additional layers of sensors in front of the ECAL to serve as a preshower detector. The calorimeter has  $e/p$  close to 1.25.
- A steel-scintillator hadronic calorimeter (HCAL) with a transverse cell size of  $5 \times 5$  cm. The depth of the HCAL in the barrel region is about 11.25 interaction lengths ( $\lambda_I$ ).<sup>2</sup> The increase in the total interaction lengths for an FCC detector compared to the LHC detectors was studied in [15]. The HCAL has 64 longitudinal layers in the barrel and the end-cap regions, which can be compared to the 40 layers of the original SiD detector. The sampling fraction of the HCAL is 3.1%. Both ECAL and HCAL can reconstruct calorimeter clusters up to  $|\eta| = 3.5$ .
- The muon system located outside the solenoid which surrounds the HCAL calorimeter. The design of this detector closely follows the original SiD proposal [3] and has an octagonal barrel geometry. The sensors cells are constructed using resistive plate chambers (RPC).
- Silicon-tungsten beam calorimeter positioned 0.52 m away from the interaction point, along the beamline.

For the studies presented below, track reconstruction was performed with the LCSim package [16] using the seed tracker algorithm used for the SiD detector [3]. Seed tracker is a generic track-finding algorithm based on a helix fitter. Tracks with  $p_T > 500$  MeV were saved for final analysis.

The GEANT4 (version 10.2) [8] was used for all results presented in this paper. As a check, low statistics event samples were created using GEANT4 10.3p1. The results were found to be consistent with the default GEANT4 10.2 used in this study. The GEANT4simulation of the calorimeter response for inelastic processes is based on the QGSP\_BERT physics list. The QGSP physics list, based on the quark-gluon string model, is used for particles in the energy range 12 GeV – 100 TeV. The validation of the QGSP physics list is available up to 400 GeV. The FTFP physics list, based on the FRITIOF model, is used for the energy range 9.5 GeV – 25 GeV, while the

---

$y$ -axis points upwards. The azimuthal angle  $\phi$  is measured around the beam axis, and the polar angle  $\theta$  is measured with respect to the  $z$ -axis. The pseudorapidity is given by  $\eta = -\ln \tan(\theta/2)$ . Transverse momentum is defined with respect to the beam axis.

<sup>2</sup>Nuclear interaction length,  $\lambda_I$ , is the average distance traveled by a hadron before undergoing an inelastic nuclear interaction.

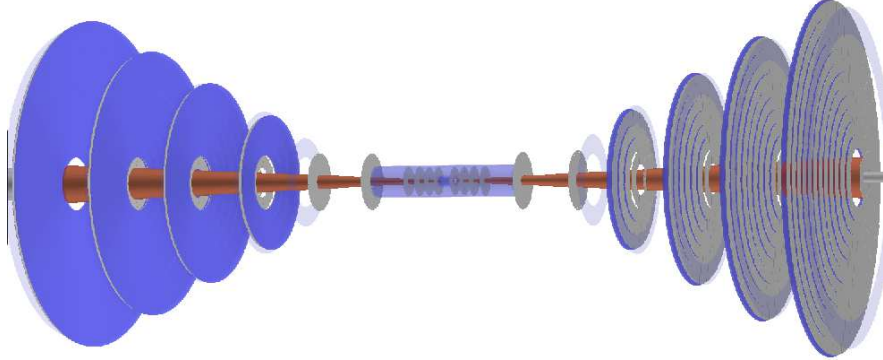


Figure 4: Illustration of the pixel and microstrip forward disks of the silicon tracker of the SiFCC detector. The barrel microstrip modules are not shown. For improved performance in the forward region, the tracker was extended in the  $z$ -direction compared to the original SiD detector.

Table 1: Technology and dimensions of the SiFCC sub-detectors in the barrel region. The solenoid field is given inside and outside the solenoid, respectively.

Barrel	Technology	pitch/cell	radii (cm)	$ z $ size (cm)
Vertex detector	silicon pixels/5 layers	$25 \mu\text{m}$	1.3 - 6.3	38
Outer tracker	silicon strips/5 layers	$50 \mu\text{m}$	39 - 209	921
ECAL	silicon pixels+W	$2 \times 2 \text{ cm}$	210 - 230	976
HCAL	scintillator+steel	$5 \times 5 \text{ cm}$	230 - 470	980
Solenoid	5 T (inner), -0.6 T (outer)	-	480 - 560	976
Muon detector	RPC+steel	$3 \times 3 \text{ cm}$	570 - 903	1400

Bertini-Cascade model applies for particles below 9.9 GeV. The elastic model ElasticHEP/Gheisha is set to be valid up to 100 TeV. Discussions of these physics lists and models together with the references can be found in the GEANT4 manual [8].

For simulations of the calorimeter response, the sampling fraction of 3.1% was used to correct hit energies in the HCAL, and the sampling fractions of 1.47% and 0.74% were used in ECAL for the respective layers. Selection cuts for calorimeter hits were applied based on the studies of the energy  $E_{mip}$  of minimum ionizing particles (mip) for single muons with the energy of 100 GeV. All hits with energy less than  $E_{mip} - 3 \cdot RMS$ , where  $RMS$  is the root mean square of the mip distribution, were rejected. In addition, hits with arrival time above 100 ns were rejected. Then the calorimeter hits are clustered using a simple cone-based clustering algorithm [17], which is also used by the PFA. We do not use the PFA for performance studies presented in this paper since it requires optimization.

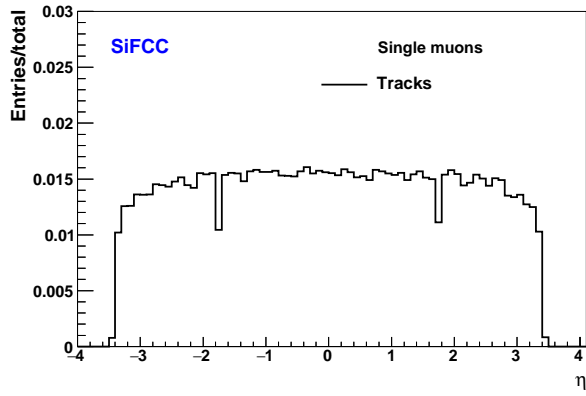
Tables 1 and 2 list the technology choices for each sub-detector of the SiFCC detector in the barrel and end-cap regions, respectively. Additional parameters related to various detector volumes can be found in the HepSim repository [13].

Figure 5 shows the pseudorapidity distributions of reconstructed tracks and calorimeter clusters. The distributions were obtained for single muons which were generated with a uniform momentum distribution between 4 GeV and 1024 GeV, and uniform

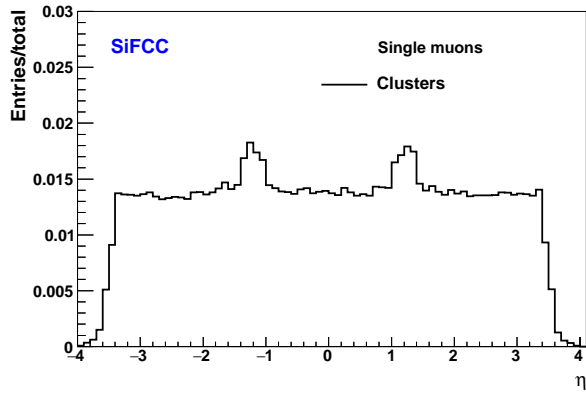
Table 2: Technology and dimensions of the SiFCC sub-detectors for the end-cap region.

End-cap	Technology	pitch/cell	$z$ extent	outer radius
			(cm)	(cm)
Vertex detector	silicon pixels	25 $\mu\text{m}$		
Outer tracker	silicon strips	50 $\mu\text{m}$		
ECAL	silicon pixels+W	2 $\times$ 2 cm	500 - 516	250
HCAL	scintillator+steel	5 $\times$ 5 cm	518 - 742	450
Muon detector	RPC+steel	3 $\times$ 3 cm	745 - 1010	895
Lumi calorimeter	silicon+W	3.5 $\times$ 3.5 mm	495 - 513	20
Beam calorimeter	semiconductor+W	3.5 $\times$ 3.5 mm	520 - 539	13

distributions in the  $-4 < \eta < 4$  range and in azimuthal angle. This figure shows the pseudorapidity range which can be used for physics analyses. The enhancement near  $|\eta| = 1.2$  for calorimeters clusters is due to the transition region between barrel and end-cap calorimeters, where the same object is reconstructed in both calorimeters and the clusters are not merged. The suppression near  $|\eta| = 1.5$  for tracks is due to the transition from the barrel to the end-cap sub-detectors of the silicon tracker.

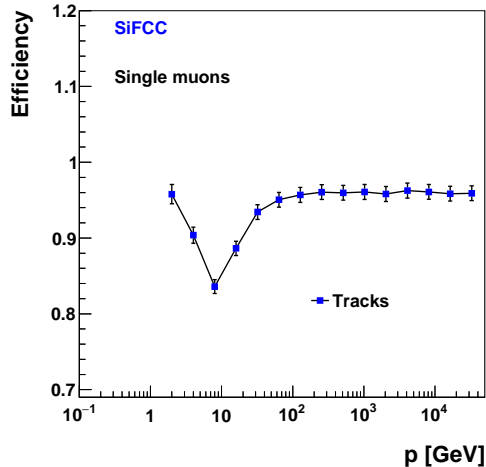


(a)  $\eta$  distribution of tracks



(b)  $\eta$  distribution of reconstructed clusters

Figure 5: The pseudorapidity distributions of reconstructed tracks and calorimeter clusters in the SiFCC detector. Single muons with uniform distributions in  $\eta$  ( $|\eta| < 4$ ) and  $\phi$ , and uniform distribution in momentum ( $p$ ) in the range  $4 < p < 1024$  GeV, were used.



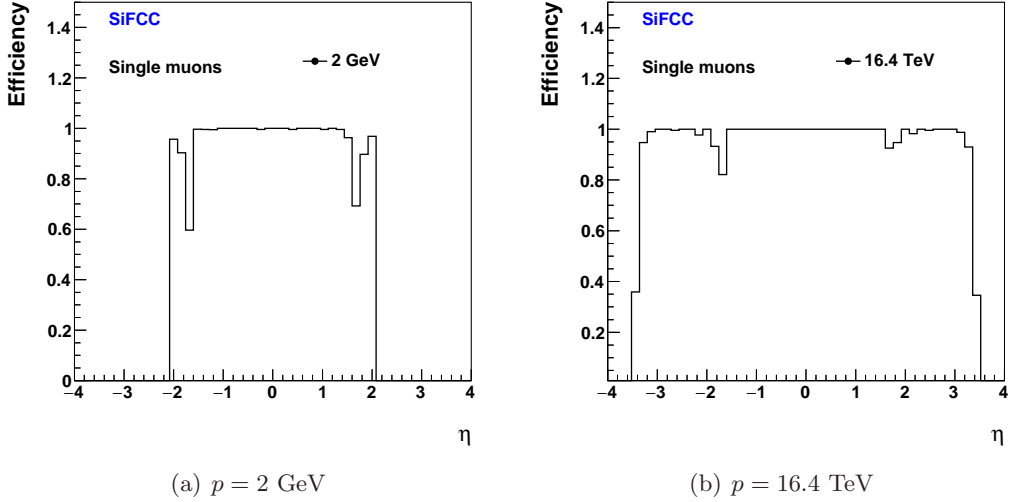


Figure 7: Tracking efficiency as a function of  $\eta$  for two different values of muon momenta  $p$ .

with the parameters  $a = 4.28 \times 10^{-3}$ ,  $b = 6.23 \times 10^{-6}/\text{GeV}$  and  $c = -4.73 \times 10^{-6}/\sqrt{\text{GeV}}$ . The fit has a good  $\chi^2/\text{ndf}$  and is shown in Fig. 8(a).

Figure 8(b) shows the fractional track  $p_T$  resolution  $\sigma(p_T)/p_T$  as a function of  $p_T$ . For this figure, the distribution of the ratio  $p_T^{\text{reco}}/p_T^{\text{true}}$  was fit using a Gaussian distribution. The width  $\sigma$  of the Gaussian was used as a measure of the fractional  $p_T$  resolution. Also shown is a fit function which can be used to parameterize the resolution for fast simulations. The fit function is

$$\frac{\sigma(p_T)}{p_T} = a + bp_T + c\sqrt{p_T} \quad (2)$$

with the fit parameters  $a = 1.76 \times 10^{-3}$ ,  $b = 5.77 \times 10^{-6}/\text{GeV}$  and  $c = -6.31 \times 10^{-5}/\sqrt{\text{GeV}}$ .

These results show that the tracking performance is within expectations for the tracking system with the given readout segmentation and the solenoid magnetic field. Further optimizations are possible after event simulation and reconstruction of the most important physics channels [18, 19].

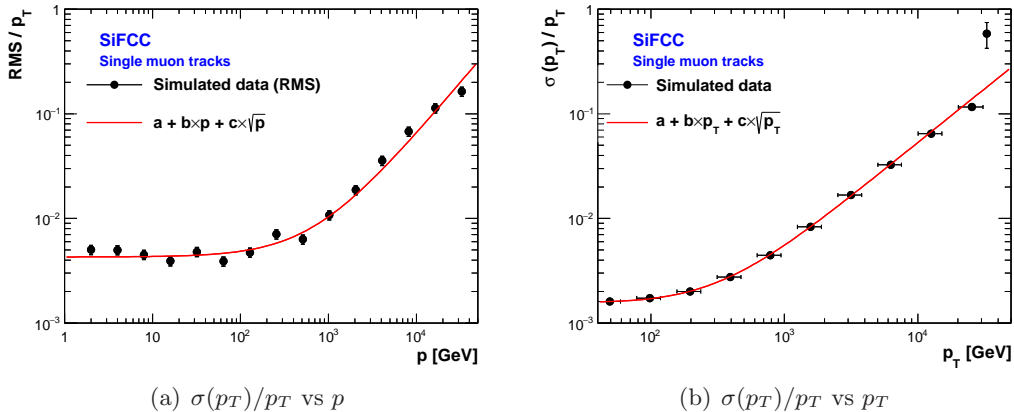


Figure 8: Fractional track  $p_T$  resolution as a function of (a)  $p$  and (b)  $p_T$ . The resolution was found using the RMS of the ratio  $p_T^{\text{reco}}/p_T^{\text{true}}$  for (a). The  $p_T$  resolution shown in (b) was determined using the width of a Gaussian fit for  $p_T^{\text{reco}}/p_T^{\text{true}}$ . The figures show the fit functions used to describe the resolutions, with the fit parameters as given in the text.

## 5. Calorimeter performance for single particles

The calorimeter response and resolution are studied by simulating single incident particles of different energies and species, as shown in Fig. 9-11. The particles were uniformly distributed in pseudorapidity and azimuthal angle. The energies of these particles were reconstructed with the anti- $k_T$  jet algorithm [20, 21] using calorimeter clusters as input. These clusters were built from calorimeter hits as explained in Sect. 3 after applying the corresponding sampling fractions. No other corrections are applied. The minimum value of the calorimeter cluster used to build jets was set to 400 MeV.

The response and resolution were calculated by matching reconstructed particles with truth-level particles, and calculating the ratio  $p_T^{\text{reco}}/p_T^{\text{true}}$ . The studies were performed in the best understood central region of  $|\eta| < 1.5$ , where the efficiency for measurements of low-momentum particles is highest. A Gaussian fit was performed to the distribution of this ratio. The response and resolution were calculated from the mean and width  $\sigma$  of the Gaussian fit, respectively. The resolution as a function of  $p_T$  was described by the following fit function:

$$\frac{\sigma(p_T)}{p_T} = a/\sqrt{p_T} \oplus b, \quad (3)$$

where  $a$  is the sampling (stochastic) term,  $b$  is the constant term and the symbol  $\oplus$  denotes a quadratic sum.

In addition to the calorimeter response, Fig. 9(left) shows the tracking resolution studied in Sect. 4. The calorimeter measurement of particle momentum above 3 TeV becomes more precise than the tracking measurement.

These studies show that the response of the calorimeter to hadrons as a function of energy is non-linear, as expected for non-compensating ECAL and HCAL calorimeters with  $e/p > 1$ . The response increases with energy, which is another expected effect for such calorimeters [22]. The response to electromagnetic particles is almost linear. The results obtained with a  $\pi^0 \rightarrow \gamma\gamma$  source were consistent with the electron and

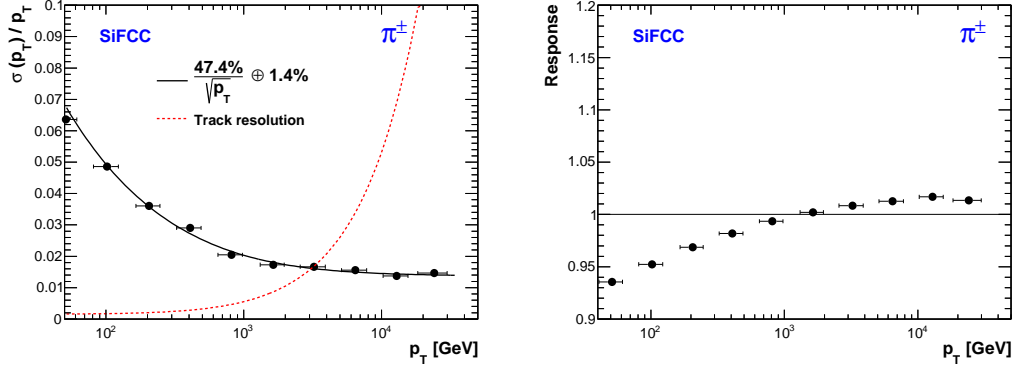


Figure 9: Calorimeter resolution (left) and response (right) to single  $\pi^\pm$  in the pseudorapidity range  $|\eta| < 1.5$ . For comparison, the dotted line shows the track fractional  $p_T$  resolution as discussed in Sect. 4.

photon results. The sampling terms are 47% and 17% respectively for hadrons and electrons/photons. The constant term of the resolution function is  $\approx 1.3\%$ , and is somewhat smaller than for an FCC calorimeter setup [15] based on the ATLAS HCAL geometry. Our studies do not indicate a leakage out the back of the hadronic calorimeter for single hadrons up to 33 TeV in transverse momentum.

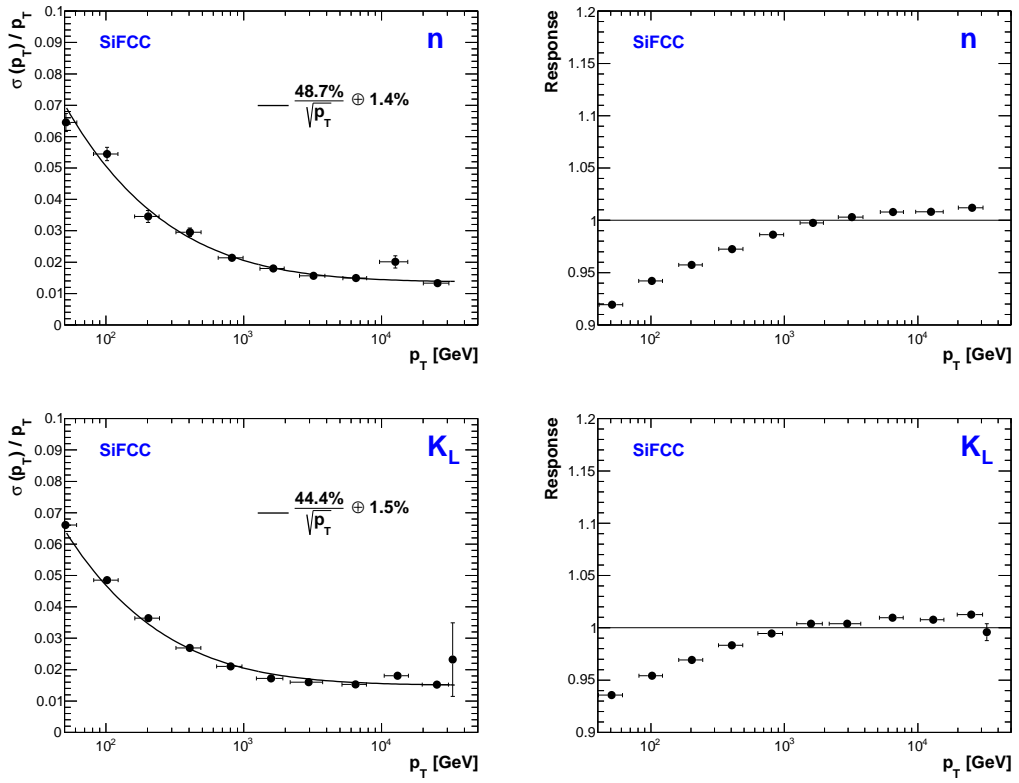


Figure 10: Calorimeter resolution (left) and response (right) to single neutrons (top) and  $K_L^0$  (bottom) in the pseudorapidity range  $|\eta| < 1.5$ .

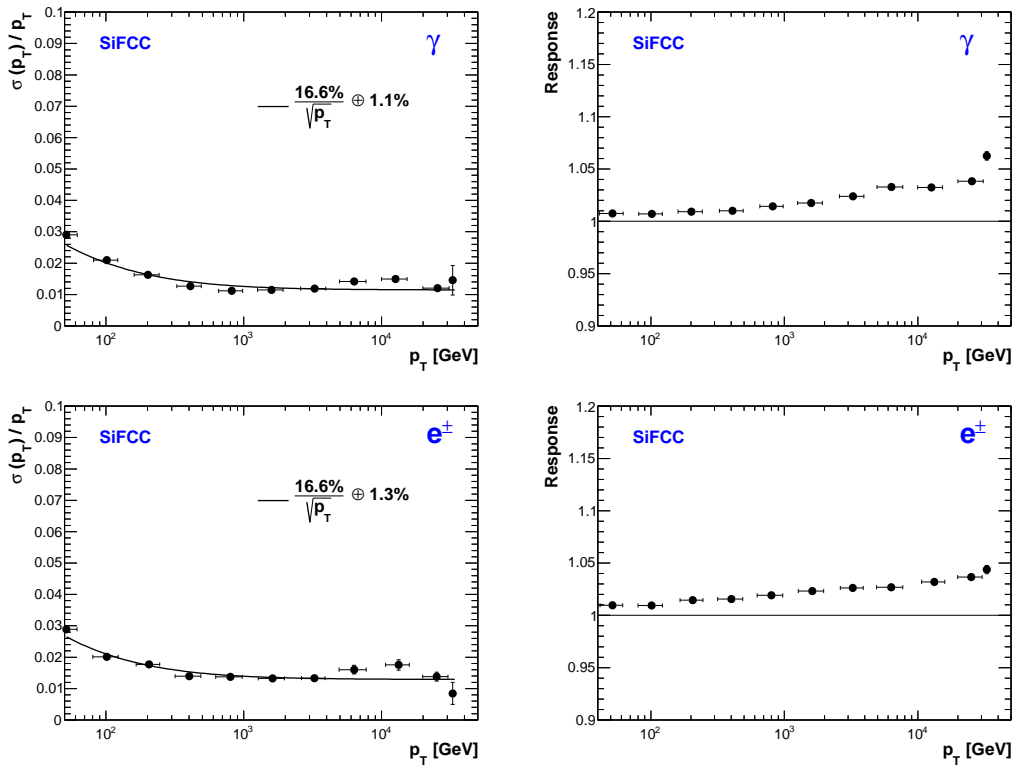


Figure 11: Calorimeter resolution (left) and response (right) to single photons (top) and electrons / positrons (bottom) in the pseudorapidity range  $|\eta| < 1.5$ .

## 6. Jet reconstruction

Many physics channels of interest at a 100 TeV pp collider require good understanding of jet reconstruction in the transverse momentum range from tens of GeV to tens of TeV. For the jet performance study using the SiFCC detector setup, QCD dijet events for 100 TeV  $pp$  collision energy were generated with the PYTHIA8 Monte Carlo generator [23]. The MSTW2008LO68cl set of parton density functions [24] was used. For jet clustering with truth-level particles as input, stable particles were selected if their mean lifetimes are larger than  $3 \cdot 10^{-11}$  seconds. Neutrinos were excluded from consideration in jet clustering.

The jets were reconstructed using the anti- $k_T$  jet algorithm [20, 21]. The distance parameter of the anti- $k_T$  jets was  $R = 0.4$  in order to make a meaningful comparison with the calorimeter-based jets of the ATLAS experiment [25]. As in the case of single particles, jets were constructed from calorimeter clusters after correcting calorimeter hits by the sampling fractions. No other corrections were used, such as those related to the non-compensating calorimeters ( $e/p > 1$ ), out of the cone leakage, dead material and others. As in the case of single-particle studies, the jet resolution and jet response were calculated in the pseudorapidity region of  $|\eta(\text{jet})| < 1.5$ .

Figure 12 shows the  $p_T^{\text{reco, jet}}/p_T^{\text{true, jet}}$  distributions, where  $p_T^{\text{reco, jet}}$  is the reconstructed jet transverse momentum and  $p_T^{\text{true, jet}}$  is the jet transverse momentum reconstructed from truth-level stable particles. Reconstructed jets and truth-level jets were matched within a distance of 0.2 defined in azimuthal angle and pseudorapidity. Figure 12 shows the  $p_T^{\text{reco, jet}}/p_T^{\text{true, jet}}$  distributions in selected ranges of jet transverse momentum, including the lowest and highest  $p_T^{\text{jet}}$  studied in this paper. The distributions have symmetric shapes which are well described by a Gaussian distribution.

The jet resolution as a function of the jet transverse momentum is shown in Figure 13(a). It was calculated using the width of the Gaussian fits illustrated in Fig. 12. The figure also shows the fit function Eq. (3) with the sampling term  $a/\sqrt{p_T^{\text{jet}}}$  and a constant term. It should be noted that a noise term, which is proportional to  $1/p_T^{\text{jet}}$ , and which is frequently discussed in the literature (see, for example, [25, 26]), was not included into the fit since it was found that the current statistical precision cannot disentangle the noise term from the sampling term.

Figure 13(a) shows that the fit function discussed above does not give a good description of the jet resolution as a function of  $p_T^{\text{jet}}$  in the transverse-momentum region from 50 GeV to 26 TeV. The observed degradation of the jet resolution for  $p_T^{\text{jet}} > 3$  TeV cannot be well described by the constant term of the fit function. Fitting the simulated data using the transverse-momentum range from 50 GeV to 2 TeV shows a better agreement of the fit function with the data, which is characterized by  $\chi^2/\text{ndf} \simeq 3$ . The jet response shown in Figure 13(b) does not depend on jet transverse momentum for  $p_T^{\text{jet}} > 1$  TeV.

It was determined that the resolution for very energetic jets is influenced by the cut on the energy and arrival time of calorimeter hits, but the effect is relatively insensitive to the pseudorapidity region and the jet size  $R$ . As a check, the selection requirements on calorimeter hits discussed in Sect. 3 were removed before the reconstruction of calorimeter clusters. Figure 14 shows that the jet resolution and response without the

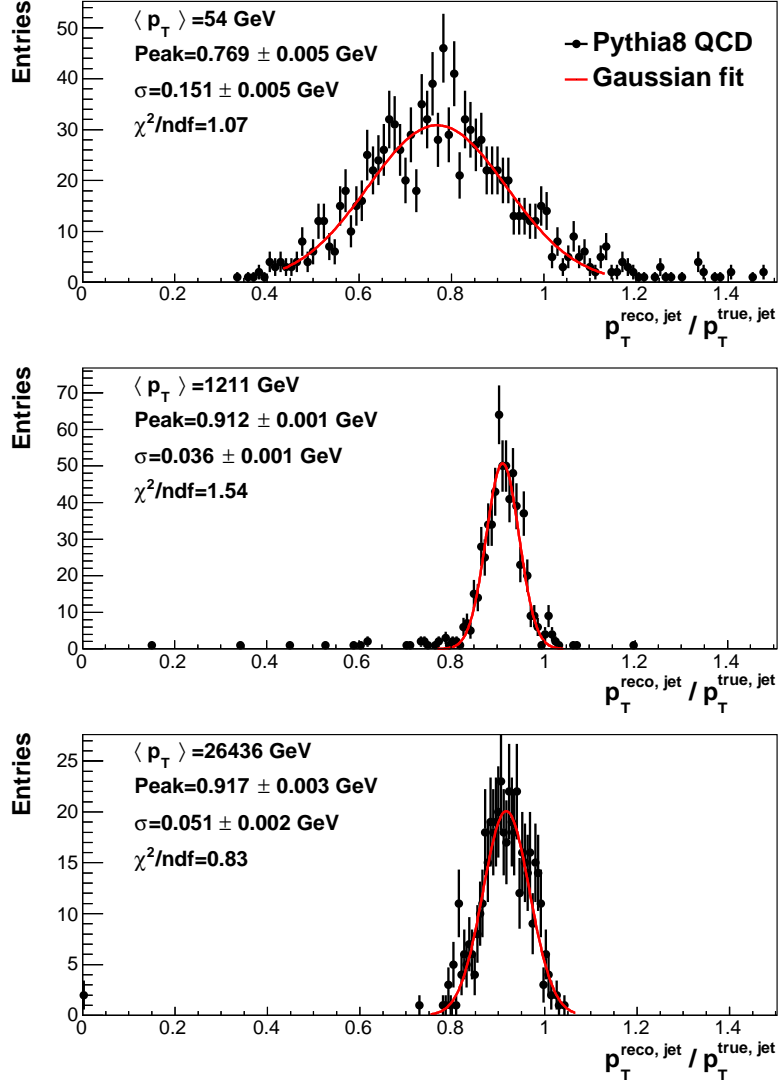


Figure 12: The distributions of  $p_T^{\text{reco, jet}} / p_T^{\text{true, jet}}$  for jets reconstructed with the anti- $k_T$  jet algorithm using the distance parameter of 0.4. The figure shows three ranges of the jet transverse momentum, together with Gaussian fits. The mean values, the Gaussian widths and the value of  $\chi^2/\text{ndf}$  of the  $\chi^2$  minimization procedure are indicated.

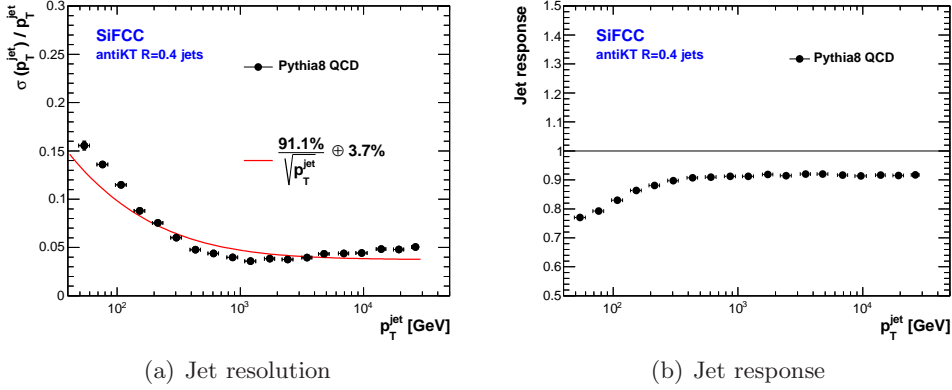


Figure 13: Resolution of anti- $k_T$  jets with the distance parameter  $R = 0.4$  as a function of jet transverse momentum calculated using the Gaussian fit. The simulated data were fitted using the resolution function from 50 GeV to 26.4 TeV (shown with the red line). Figure (b) shows the jet response using the Gaussian fits for determination of the mean values of the  $p_T^{\text{reco, jet}}/p_T^{\text{true, jet}}$  distribution. The studies were performed using the PYTHIA8 Monte Carlo generator for  $pp$  collision events at 100 TeV after simulation of the SiFCC detector response.

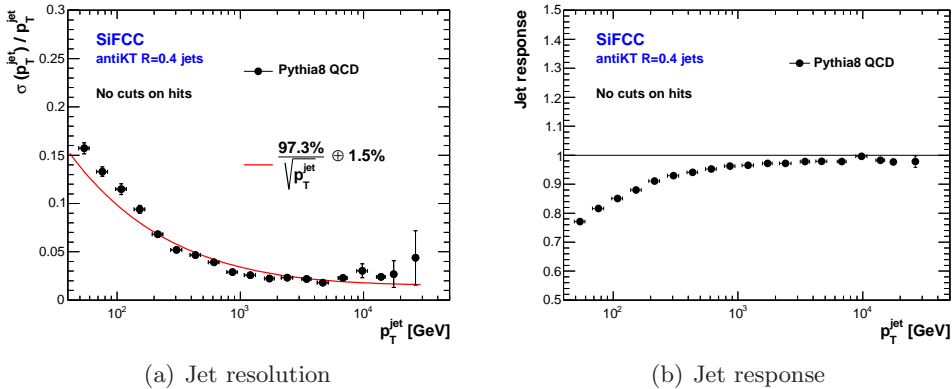


Figure 14: Same as Figure 13, but without the minimum energy and maximum time requirements on the calorimeter hits used for creating calorimeter clusters.

hit requirements are significantly improved for high- $p_T^{\text{jet}}$  jets, compared to the standard cluster reconstruction.

The results presented in Figs 13 and 14 indicate a promising quality of jet reconstruction by the SiFCC detector, with the estimated jet resolution similar to a typical resolution for calorimeter-based jets of the ATLAS experiment in the region below 1 TeV. For example, the fractional jet resolution of anti- $k_T$  jets with  $R = 0.4$  for the ATLAS experiment [25] is about 0.1 for  $p_T^{\text{jet}} \simeq 100$  GeV and 0.05 for jets with  $p_T^{\text{jet}} \simeq 0.5$  TeV, which is similar to the resolution shown in Fig. 13.

These initial studies provide a first glimpse of jet reconstruction in the energy range of tens of TeV. The main conclusion of this study is that the constant term below 5% is achievable for calorimeter-based jets with transverse momentum above 26 TeV using the detector setup discussed in this paper. A significant improvement for the jet-energy resolution at transverse momentum below 0.5 TeV is expected for the PFA approach.

## 7. Double-particle studies

A key consideration for hadronic calorimeters for future collider detectors is the impact of granularity on resolving energy deposits from pileup vertices and highly-boosted jet topologies. This understanding will be extremely important for measuring jet substructure for highly-boosted heavy objects such as  $W$ ,  $Z$  and  $H$  bosons and top quarks. Hadronic calorimeters currently in use have cell sizes which are larger than the nuclear interaction length,  $\lambda_I$ . In this section, the use of smaller cell sizes to resolve individual hadrons is investigated.

To study the effect of calorimeter granularity on hadron reconstruction, the density of energy reconstructed in calorimeter cells was investigated for events with pairs of  $K_L^0$  produced at various angular separations. Since these neutral hadrons provide no tracking information, their position and energy measurements can only be obtained from calorimetry. Double- $K_L^0$  samples are simulated with energies of 100 GeV or 1000 GeV for both particles. Each event has two particles separated by an azimuthal angle,  $\Delta\phi^K$ , keeping  $\eta^K = 0$  for both particles. The particles are separated in multiples of  $0.5^\circ$  (about 0.009 rad), starting from  $\Delta\phi^K = 0$ , and stepping them apart until they have the separation of  $10^\circ$ .

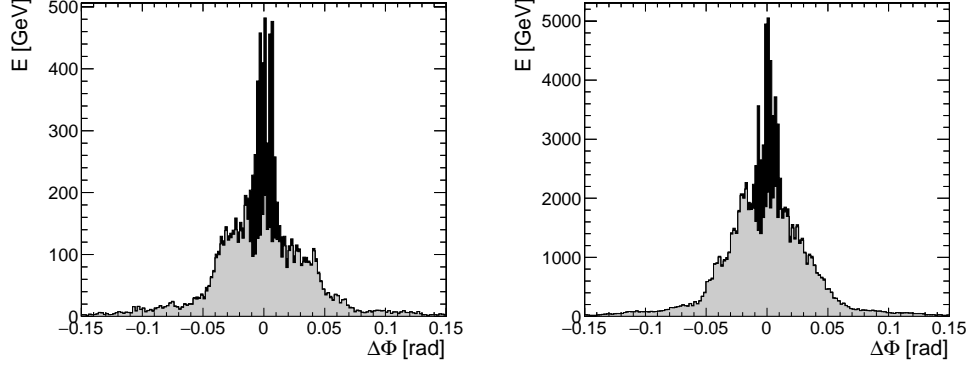
The ECAL and HCAL granularities were changed to understand its impact on resolving the two  $K_L^0$  showers. We plot the energy-weighted distribution of calorimeter cells in the azimuthal angle  $\Phi$  for a fixed  $K_L^0$  angular separation, as shown in Fig. 15-18 for  $K_L^0$  angular separations  $\Delta\phi^K$  in the range 0.009 – 0.104 rad and for three calorimeter cell sizes. The energies of cells were reconstructed from the sum of the corresponding calorimeter hits, after applying the sampling fractions. The ECAL cell size is  $2 \times 2$  cm when HCAL cell sizes are  $20 \times 20$  cm (configuration I) and  $5 \times 5$  cm (configuration II). The ECAL cell size is  $3 \times 3$  mm when the HCAL cell size is  $1 \times 1$  cm (configuration III). The distributions are integrated over 50 events.

We find that as we improve granularity, the spatial resolving power of hadronic showers increases. To set the physical scale of the angular separation from boosted jets, we consider a boosted  $W$ ,  $Z$  or Higgs boson with  $p_T \sim 10$  TeV, producing decay quarks with a typical opening angle of 0.001 rad. Figure 15 shows the calorimeter response of two  $K_L^0$  particles with an angular separation of  $\Delta\phi^K = 0.009$  rad. The hadrons are resolved in the ECAL of configuration III. Doubling the  $K_L^0$  separation to  $\Delta\phi^K = 0.018$  rad results in the hadrons being resolved in the ECAL of all three configurations, and the HCAL of configuration III, as shown in Fig. 16. Further increasing the  $K_L^0$  separation to 0.035 rad results in them being resolved in the HCAL of configuration II, but not in configuration I (which is the current practice in HEP detectors such as CMS), as shown in Fig. 17. Finally, it is shown in Fig. 18 that the HCAL of configuration I can resolve hadrons with separation in the 0.07-0.1 rad range.

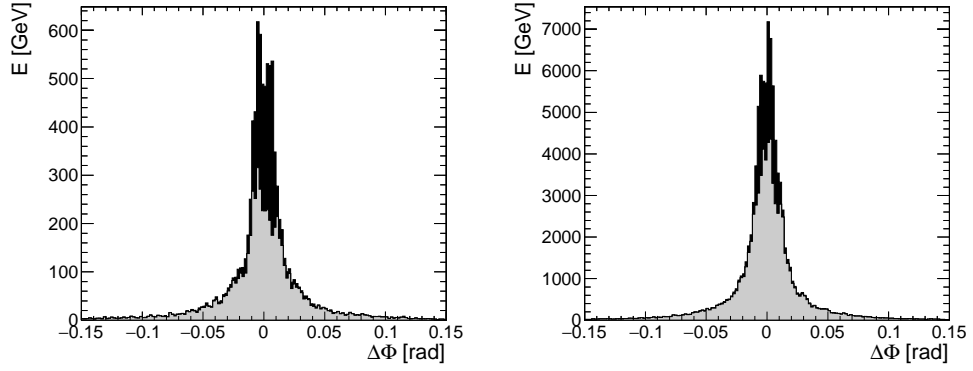
The energy-dependence of the spatial resolving power is also illustrated in these figures. In the hadron energy range of 100 – 1000 GeV, the energy dependence is weak, but noticeable in the HCAL.

These results can lead to an understanding of how well hadrons can be resolved on an event-by-event basis. Figures 15-18 indicate that one can resolve individual hadron showers at smaller separation than the nuclear interaction length (18 cm for steel, corresponding to angular separation of 0.08 rad at a radius of 230 cm). The

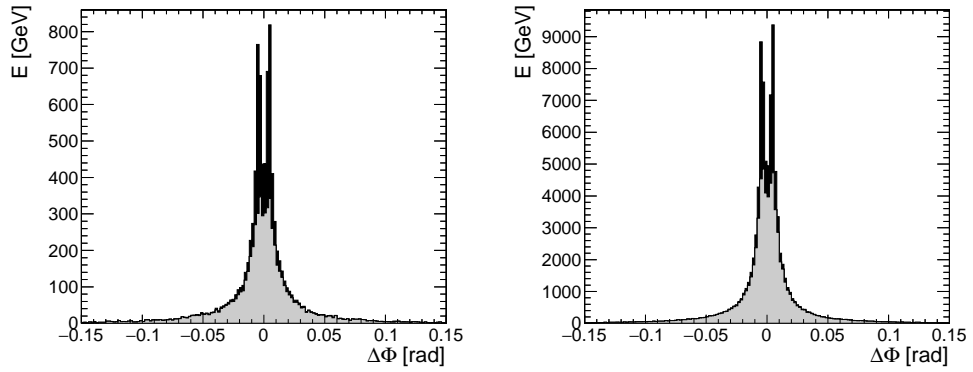
studies at the high energies presented here go beyond those performed by the CALICE collaboration [\[27\]](#).



(a)  $20 \times 20$  cm HCAL cells and  $2 \times 2$  cm ECAL cells

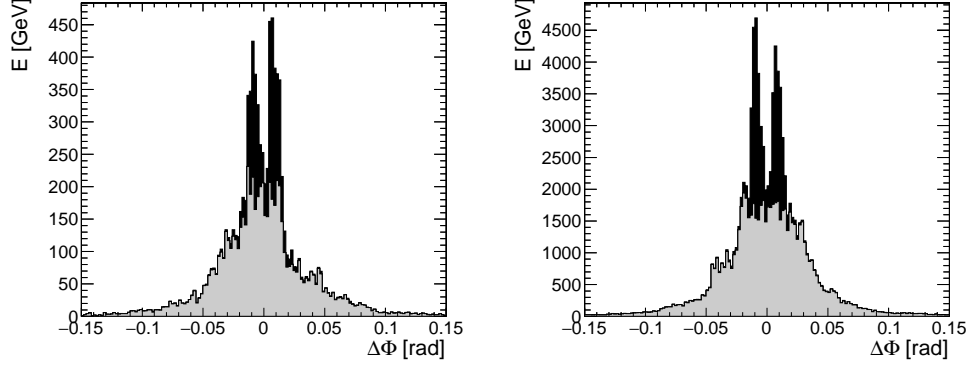


(b)  $5 \times 5$  cm HCAL cells and  $2 \times 2$  cm ECAL cells

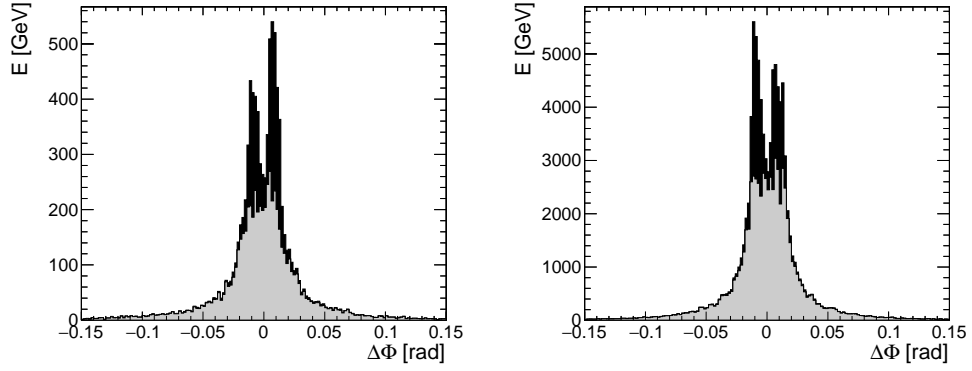


(c)  $1 \times 1$  cm HCAL cells and  $3 \times 3$  mm ECAL cells

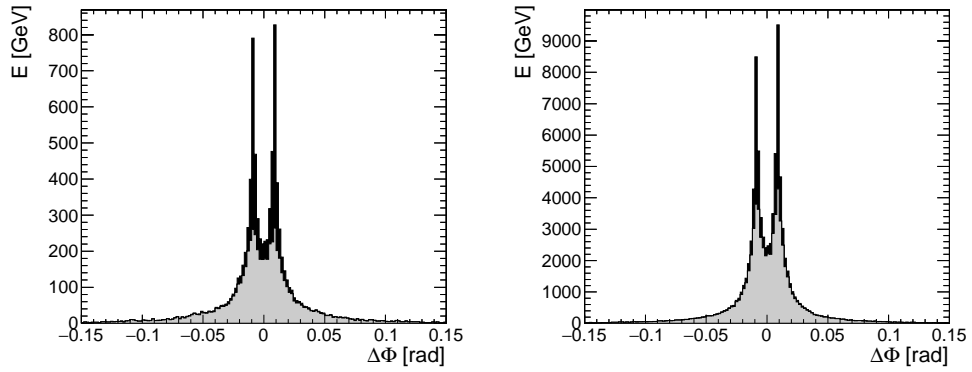
Figure 15: Azimuthal distribution of energy deposition for pair of incident  $K_L^0$  particles at 100 GeV (left) and 1000 GeV (right), with the angular separation of  $\Delta\phi^K = 0.009$  rad. Electromagnetic calorimeter cells are indicated in black while hadronic calorimeter cells are indicated in gray.



(a)  $20 \times 20$  cm HCAL cells and  $2 \times 2$  cm ECAL cells

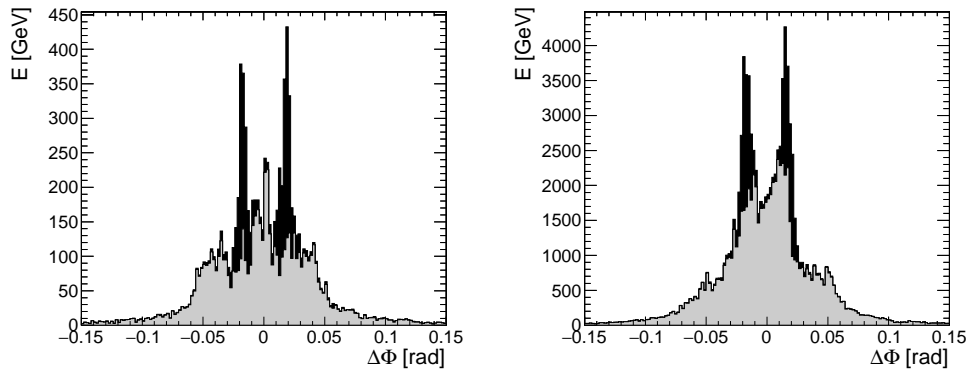


(b)  $5 \times 5$  cm HCAL cells and  $2 \times 2$  cm ECAL cells

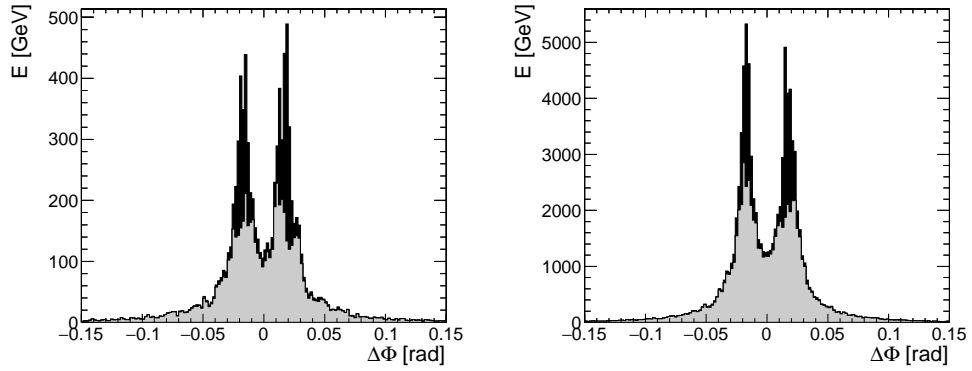


(c)  $1 \times 1$  cm HCAL cells and  $3 \times 3$  mm ECAL cells

Figure 16: Azimuthal distribution of energy deposition for pair of incident  $K_L^0$  particles at 100 GeV (left) and 1000 GeV (right), with the angular separation of  $\Delta\phi^K = 0.018$  rad. Electromagnetic calorimeter cells are indicated in black while hadronic calorimeter cells are indicated in gray.

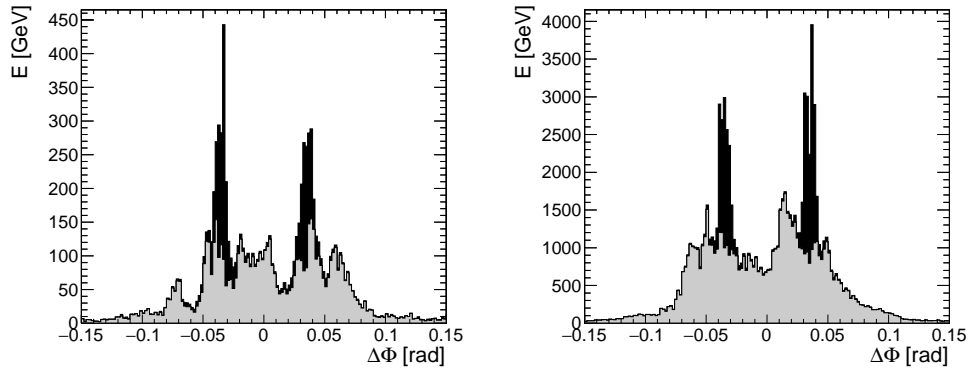


(a)  $20 \times 20$  cm HCAL cells and  $2 \times 2$  cm ECAL cells

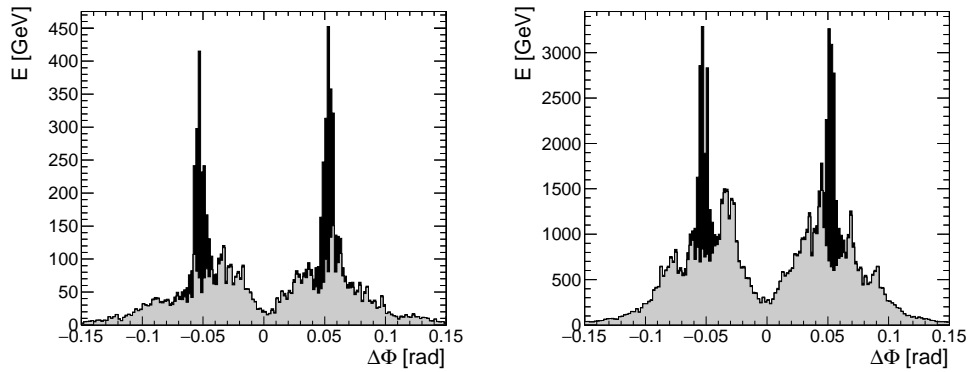


(b)  $5 \times 5$  cm HCAL cells and  $2 \times 2$  cm ECAL cells

Figure 17: Azimuthal distribution of energy deposition for pair of incident  $K_L^0$  particles at 100 GeV (left) and 1000 GeV (right), with the angular separation of  $\Delta\phi^K = 0.035$  rad. Electromagnetic calorimeter cells are indicated in black while hadronic calorimeter cells are indicated in gray.



(a)  $K_L^0$  angular separation of 0.069 rad.



(b)  $K_L^0$  angular separation of 0.104 rad.

Figure 18: Azimuthal distribution of energy deposition for pair of incident  $K_L^0$  particles at 100 GeV (left) and 1000 GeV (right), for a calorimeter with  $20 \times 20$  cm HCAL cells and  $2 \times 2$  cm ECAL cells. The distributions are shown for the incident  $K_L^0$  angular separations of (a) 0.069 rad and (b) 0.104 rad. Electromagnetic calorimeter cells are indicated in black while hadronic calorimeter cells are indicated in gray.

## 8. Summary

A detector has been designed to study the physics performance at the energy scale of the FCC-hh or SppC collider. The concept of the SiFCC detector has been presented for the first time, as well as detailed characteristics relevant for multi-TeV physics. The performance of this detector has been illustrated using GEANT4-based Monte Carlo simulations of single incident particles of different species. It is shown that the tracking and calorimeter performance achieved with this initial general-purpose detector concept meets our expectations for the given technology choices. The resolution and reconstruction efficiency of single particles are well within the expected specifications. No significant leakage out the back of the hadronic calorimeter is observed for single hadrons up to 33 TeV in transverse momentum.

Transverse momentum resolution of jets reconstructed from energy deposits in the calorimeters is close to 5% for jets with transverse momenta above 26 TeV. For the current detector setup, the study indicates a degradation of jet resolution for  $p_T^{\text{jet}} > 3$  TeV. The jet response saturates at a value about 10% below unity for  $p_T^{\text{jet}} > 1$  TeV. Both effects depend on requirements for the calorimeter hits, such as the minimum hit energy and hit arrival time. Removal of the hit requirements eliminates the degradation of resolution and recovers the response, which tends to unity for  $p_T^{\text{jet}} > 3$  TeV. To this day, this is the first estimate of jet resolution and response for jets in the  $p_T^{\text{jet}}$  range of tens of TeV using a GEANT4-based simulation followed by realistic event reconstruction.

The study of double hadrons with small angular separation illustrates that hadronic showers of close-by particles can be resolved by using a high-granularity calorimeter. These results go beyond the studies performed for the ILC by the CALICE Collaboration in the context of particle flow algorithms. We believe that our observations help pave the way for using high-granularity calorimeters for the reconstruction of multi-TeV jets and particles at future colliders.

Using this detector concept, various Monte Carlo event samples covering a wide range of physics processes have been made available in the HepSim data repository [13]. In the future, optimized designs of this detector will be introduced after analysis of simulated events of the most important physics channels [18, 19] for 100 TeV  $pp$  collisions.

## Acknowledgements

This research was performed using resources provided by the Open Science Grid, which is supported by the National Science Foundation and the U.S. Department of Energy's Office of Science. We gratefully acknowledge the computing resources provided on Blues, a high-performance computing cluster operated by the Laboratory Computing Resource Center at Argonne National Laboratory. Argonne National Laboratory's work was supported by the U.S. Department of Energy, Office of Science under contract DE-AC02-06CH11357. The Fermi National Accelerator Laboratory (Fermilab) is operated by Fermi Research Alliance, LLC under Contract No. DE-AC02-07CH11359 with the United States Department of Energy.

## References

- [1] M. Benedikt, [The Global Future Circular Colliders Effort](#) CERN-ACC-SLIDES-2016-0016. Presented at P5 Workshop on the Future of High Energy Physics, BNL, USA, Dec. 15-18, 2013. URL <http://cds.cern.ch/record/2206376>
- [2] J. Tang, et al., Concept for a Future Super Proton-Proton Collider (2015). [arXiv:1507.03224](#).
- [3] H. Aihara, et al., SiD Letter of Intent, 2009, presented to ILC IDAG. [arXiv:0911.0006](#).
- [4] C. Adolphsen, et al., The International Linear Collider Technical Design Report - Volume 3. II: Accelerator Baseline Design, 2013. [arXiv:1306.6328](#).
- [5] H. Abramowicz, et al., The International Linear Collider Technical Design Report - Volume 4: Detectors, 2013. [arXiv:1306.6329](#).
- [6] M. J. Charles, PFA Performance for SiD, in: Linear colliders. Proceedings, International Linear Collider Workshop, LCWS08, and International Linear Collider Meeting, ILC08, Chicago, USA, November 16-20, 2008, 2009. [arXiv:0901.4670](#).
- [7] J. S. Marshall, M. A. Thomson, Pandora Particle Flow Algorithm, in: Proceedings, International Conference on Calorimetry for the High Energy Frontier (CHEF 2013), 2013, pp. 305–315. [arXiv:1308.4537](#).
- [8] J. Allison, et al., Recent developments in Geant4, Nuclear Instruments and Methods in Physics Research A 835 (2016) 186.
- [9] N. Graf, J. McCormick, Simulator for the linear collider (SLIC): A tool for ILC detector simulations, AIP Conf. Proc. 867 (2006) 503–512.
- [10] DELPHES 3 Collaboration, J. de Favereau, et al., DELPHES 3, A modular framework for fast simulation of a generic collider experiment, JHEP 1402 (2014) 057. [arXiv:1307.6346](#).
- [11] S. V. Chekanov, E. May, K. Strand, P. Van Gemmeren, ProMC: Input-output data format for HEP applications using varint encoding, Comp. Phys. Commun. 185 (2013) 2629–2635, aNL-HEP-CP-13-32. [arXiv:1311.1229](#).
- [12] S. V. Chekanov, Public repository with Monte Carlo simulations for high-energy particle collision experiments, in: 38th International Conference on High Energy Physics (ICHEP 2016) Chicago, IL, USA, August 03-10, 2016, 2016, PoS (ICHEP2016) 229. [arXiv:1609.04455](#).
- [13] S. Chekanov, HepSim: a repository with predictions for high-energy physics experiments, Advances in High Energy Physics 2015 (2015) 136093, available as <http://atlaswww.hep.anl.gov/hepsim/>.
- [14] R. Pordes, et al., The Open Science Grid, J. Phys. Conf. Ser. 78 (2007) 012057.
- [15] T. Carli, C. Hulsens, A. Henriques Correia, C. Solans Sanchez, Containment and resolution of hadronic showers at the FCC, JINST 11 (09) (2016) P09012. [arXiv:1604.01415](#).
- [16] N. Graf, J. McCormick, LCSIM: A detector response simulation toolkit, in: 2012 IEEE Nuclear Science Symposium and Medical Imaging Conference Record (NSS/MIC), 2012, p. 1016.
- [17] M. Thomson, Particle flow calorimetry and the PandoraPFA algorithm, Nuclear Instruments and Methods in Physics Research Section A: Accelerators, Spectrometers, Detectors and Associated Equipment 611 (1) (2009) 25 – 40.
- [18] M. L. Mangano, et al., Physics at a 100 TeV pp collider: Standard Model processes CERN-TH-2016-112, FERMILAB-FN-1021-T. [arXiv:1607.01831](#).
- [19] R. Contino, et al., Physics at a 100 TeV pp collider: Higgs and EW symmetry breaking studies CERN-TH-2016-113. [arXiv:1606.09408](#).
- [20] M. Cacciari, G. P. Salam, G. Soyez, The anti-kt jet clustering algorithm, JHEP 0804 (2008) 063. [arXiv:0802.1189](#).
- [21] S. Catani, Y. L. Dokshitzer, M. H. Seymour, B. R. Webber, Longitudinally invariant  $K_t$  clustering algorithms for hadron hadron collisions, Nucl. Phys. B406 (1993) 187.
- [22] R. Wigmans, Effects of calorimeter peculiarities on the jet energy scale, J. Phys. Conf. Ser. 323 (2011) 012001.
- [23] T. Sjostrand, S. Mrenna, P. Z. Skands, PYTHIA 6.4 Physics and Manual, JHEP 05 (2006) 026. [arXiv:hep-ph/0603175](#).
- [24] A. Martin, W. Stirling, R. Thorne, G. Watt, Parton distributions for the LHC, Eur. Phys. J. C63 (2009) 189–285. [arXiv:0901.0002](#), [doi:10.1140/epjc/s10052-009-1072-5](#).
- [25] ATLAS Collaboration, G. Aad, et al., Jet energy resolution in proton-proton collisions at  $\sqrt{s} = 7$  TeV recorded in 2010 with the ATLAS detector, Eur. Phys. J. C73 (3) (2013) 2306. [arXiv:1210.6210](#), [doi:10.1140/epjc/s10052-013-2306-0](#).
- [26] R. Calkins, et al., Reconstructing top quarks at the upgraded LHC and at future accelerators, in:

Proceedings, Community Summer Study 2013: Snowmass on the Mississippi (CSS2013): Minneapolis, MN, USA, July 29-August 6, 2013. [arXiv:1307.6908](#).

URL <https://inspirehep.net/record/1244676/files/arXiv:1307.6908.pdf>

- [27] CALICE Collaboration, C. Adloff, et al., Tests of a particle flow algorithm with CALICE test beam data, JINST 6 (2011) P07005. [arXiv:1105.3417](#).